JTTEE5 15:545-552
DOI: 10.1361/105996306X147216
1059-9630/$19.00 © ASM International

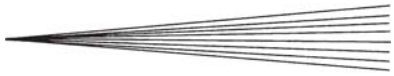

Modeling Thermal Conductivity of Thermal Spray Coatings: Comparing Predictions to Experiments

Y. Tan, J.P. Longtin, and S. Sampath

(Submitted February 28, 2006; in revised form July 7, 2006)

Thermal conductivity plays a critical role in the thermal transport of thermal-sprayed coatings. In this article, a combined image analysis and finite-element method approach is developed to assess thermal conductivity from high-resolution scanning electron microscopy images of the coating microstructure. Images are analyzed with a collection of image-processing algorithms to reveal the microscopic coating morphology. The processed digital image is used to generate a two-dimensional finite-element mesh in which pores, cracks, and the bulk coating material are identified. The effective thermal conductivity is then simulated using a commercial finite-element code. Results are presented for three coating material systems [yttria-stabilized zirconia (YSZ), molybdenum, and NiAl], and the results are found to be in good agreement with the experimental values obtained using the laser flash method. The YSZ coatings are also annealed, and the analysis procedure was repeated to determine whether the technique can accurately assess changes in coating morphology.

Keywords finite element, image analysis, molybdenum, NiAl, thermal conductivity, thermal spray coatings, yttria-stabilized zirconia

1. Introduction

Thermal spray can produce many different coatings and surfaces with various materials to protect engineering structures from wear, corrosion, erosion, and excessive temperature (Ref 1). Thermal spray coatings are produced by a continuous melt-spray-solidify process in which molten particles are accelerated and applied by impact onto a substrate to form thin splats that build up to a well-bonded deposit (Ref 2). The resulting coating properties strongly depend on the coating microstructure for all constituents, including feedstock material, air, oxide, impurities, and contaminations.

The thermal conductivity of a coating often depends very strongly on feedstock material and process parameters. In many cases, the coating thermal properties may be considerably different than the corresponding bulk material (Ref 3), especially for metal coatings (Ref 4). There has been extensive analytical, numerical, and experimental work on properties, microstructures, and their correlation for two- and three-phase composite porous media to understand and predict coating thermal properties. For analytical modeling, McPherson (Ref 3) and Cernuschi et al. (Ref 5) developed geometric models to estimate the ratio of the coating and the bulk material thermal conductivity. Sevostianov and Kachanov (Ref 6) calculated the thermal conductivities of coatings in terms of the relevant microstructural parameters.

In terms of numerical simulation, our group has previously developed property estimation methods based on both the image-based finite-element method for scanning electron microscopy (SEM) images and the use of statistically similar coating models based on small-angle-neutron scattering (SANS) (Ref 7). Deshpande et al. (Ref 8) and Kulkarni et al. (Ref 9) developed image analysis (IA) techniques to estimate porosity and thermal conductivity in thermal spray coatings. Other researchers have also addressed this as well. Lavigne et al. (Ref 10) used image-analysis techniques to estimate the porosity of coatings, and subsequently Poulain et al. (Ref 11) used an image-based technique and a finite-difference approach to estimate thermal conductivity from the coating cross-sectional images.

In this work, the authors present an IA-based estimation technique for determining the thermal conductivity of thermal spray coatings. As performed by Poulain et al. (Ref 11), the digitized image forms the basis for the computational domain. Finite-element analysis (FEA) is used to simulate the thermal transport in the coating based on the image, and the effective thermal conductivity is calculated.

Making accurate model predictions is complicated by the fact that reported experimental values can vary from coating to coating, depending on the deposition technique, heat treatment, and thermal cycling (Ref 12-14). Even for bulk materials of the same composition, the variance in property measurement data can be large (Ref 14-16). This work complements other modeling efforts made by our group, such as the FEA and SANS (Ref 7), and IA (Ref 8, 9) approaches, by incorporating pixel-based FEA modeling and pore and crack separation based on IA. The goal was to assess coating properties with improved accuracy while providing insight into the mechanisms governing transport in coatings.

This article was originally published in *Building on 100 Years of Success: Proceedings of the 2006 International Thermal Spray Conference* (Seattle, WA), May 15-18, 2006, B.R. Marple, M.M. Hyland, Y.-Ch. Lau, R.S. Lima, and J. Voyer, Ed., ASM International, Materials Park, 2006.

Y. Tan and **J.P. Longtin,** Department of Mechanical Engineering; and **S. Sampath,** Department of Material Science and Engineering, State University of New York at Stony Brook, Stony Brook, New York 11794-2300. Contact e-mail: jlongtin@ms.cc.sunysb.edu.

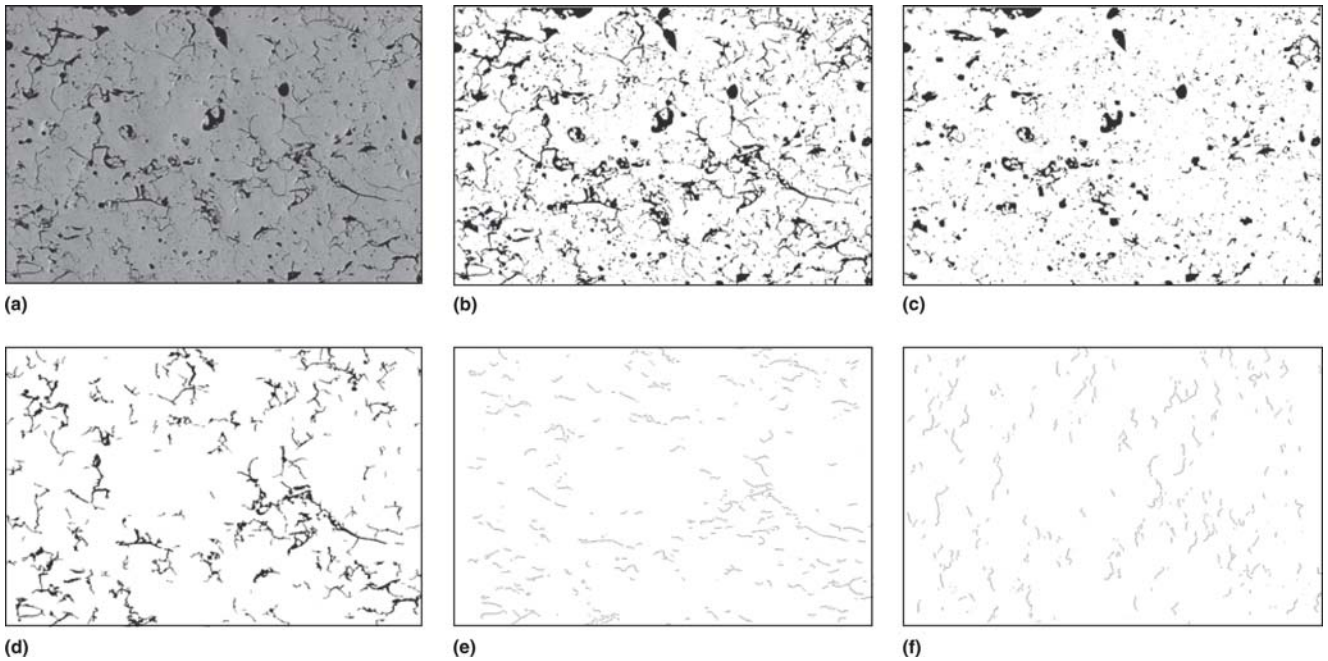

Fig. 1 (a) An original grayscale SEM image for a zirconia-based ceramic coating, (b) binary or black-and-white image, (c) globular pore image, (d) crack image, (e) horizontal crack image, and (f) vertical crack image

The coating systems studied in this work include yttria-stabilized zirconia (YSZ), pure Mo, and Ni-5wt.%Al. Thermal conductivity modeling and experiments are performed for all three coating systems. The major application of YSZ coatings is for thermal barrier coatings (TBC), among which, the 6 to 8 wt.% yttria content YSZ coating has been widely used. A 1 to 2 mm thick YSZ coating can drop the temperature of the superalloy substrate in a turbine engine by 100 to 300 °C and can greatly increase the thermodynamic efficiency (Ref 17). Molybdenum coatings fabricated by atmospheric plasma spraying have enhanced resistance to wear and heat (Ref 18). Ni-5wt.%Al coatings are used as bond coats due to their superior adhesion (Ref 19).

Image analysis is a powerful tool in pore and crack network analysis. In this article, the microstructure of thermal spray coatings, including volume fraction (porosity), aspect ratio, and crack orientations, is investigated through an IA technique that was originally developed by Friis (Ref 20). Most nonmetallic coatings, such as YSZ ceramic coatings, can be considered as two-phase composite materials, with the two phases being ceramic and air. The effective medium theory was first introduced by Maxwell-Garnett (Ref 21) to estimate the thermal conductivity of binary mixtures. Most current models consider two issues, namely, the volume fraction (i.e., the porosity) and the orientation of pores and cracks. In YSZ coatings, the splats are separated by pores and cracks due to rapid solidification. Bulk YSZ already has a low thermal conductivity ranging from 2 to 6 W/m/K depending on grain size and yttria content. The existence of the pore and crack network reduces the thermal conductivity of a YSZ coating even lower, in some cases reaching only 25% of that of the bulk material (Ref 3, 15).

In contrast to nonmetals, metals usually have high thermal conductivity and are easily oxidized. The oxide in the coating represents a third constituent that can influence the coating properties. In this article, the oxidation components are not distinguished from pores and cracks. The thermal conductivity of the oxides is generally lower than that of the corresponding metals (Ref 22).

2. Coating Image Collection and Analysis

SEM provides high-resolution microstructure images compared with those provided by optical microscopy, and a LEO 1550 SFEG (Oberkochen, Germany) scanning electron microscope is used for imaging at magnifications between ×500 and ×5000 in this work. Thermal spray coatings are cut and polished on the cross section. The raw and uncompressed images from the scanning electron microscope SEM are collected using the backscattering detector are 8-bit grayscale images in TIFF format. The resolution of the SEM image is 1024 × 768 pixels, which is the same as the resolution of the detector in the scanning electron microscope.

A public domain IA software from the National Institutes of Health (NIH) (Ref 23) (NIH Image, version 1.62) is used to transform grayscale images to binary (black and white) images, by setting a thresholding criterion based on the gray level mismatch between the YSZ matrix and the void matrix (Ref 24). The thresholding criterion is determined automatically by the software, which influences the resulting binary images and thus the finite-element modeling results.

As an example, Fig. 1(a) shows an SEM image of a YSZ coating that is 170 × 108 μm in actual size. The top and bottom of the image correspond to the top (exposed) and bottom (substrate) region of the coating, respectively. The coating microstructure images were converted from 0 to 255 grayscale to a 0-1 binary scaling using the NIH IA software, through which the detailed topology information was recorded for every pore and interlaminar crack inside the coating. The binary image of Fig. 1(a) is shown in Fig. 1(b). The black pixels in Fig. 1(b) represent

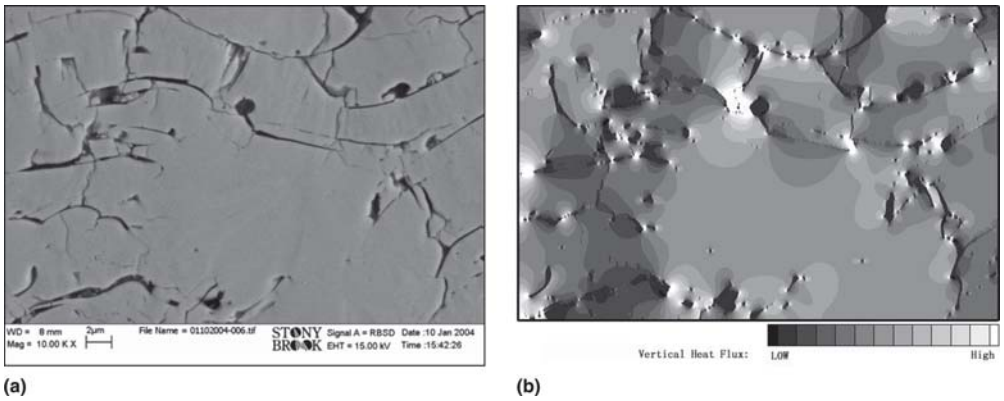

Fig. 2 (a) Original SEM image of YSZ coating, (b) vertical heat flux counter. Black and white represent the lowest and highest heat fluxes, respectively.

voids, and the white pixels represent ceramic. In Fig. 1(c) and (d), individual pores and cracks are identified based on their aspect ratio. Each shape is considered to be a spheroidal element with aspect ratios of *h:w*, where *w* and *h* are the major and minor axes, respectively. The object is taken to be a globular pore if its aspect ratio is greater than or equal to a constant (in Fig. 1, the constant is 1/6), and is taken as a crack if its aspect ratio is less than this constant. Change to the constant can vary the separated images shown in Fig. 1(c) and (d). This separation technique, which was originally developed by Friis (Ref 20), is not required for thermal conductivity modeling in this work. However, it allows insights into the coating microstructure. Moreover, each single crack is analyzed and classified as horizontal or vertical with respect to the angle between the cracks and the horizontal boundary of the image, with a thresholding angle of 45°. Images of the horizontal and vertical cracks are shown in Fig. 1(e) and (f), respectively.

2.1 Threshold Variability

To investigate the threshold variability, a group of 60 grayscale SEM images of YSZ coatings are analyzed using the NIH software. These images were obtained using the same SEM instrument but are at varying magnifications from ×1000 to ×10000. The standard deviation of the threshold values of the 60 images is 5%.

3. Image-Based Finite Element Property Modeling

In this article, the IA results are used directly to generate the material property matrices in a finite-element simulation Thermal conductivity modeling results are provided for both through-thickness and in-plane directions for a single image.

The image in Fig. 1(b) is a binary image with $m \times n$ pixels (*m* represents rows and *n* represents columns), where black represents a void and white represents the coating (e.g., YSZ in this image). This image can be used directly as the calculation mesh for an FEA. The resulting image produces a mesh with *m* rows and *n* columns, with 0 representing a void and 1 representing the coating material (e.g., YSZ). Ansys, version 8.0 (Canonsburg, PA), is used for all FEAs.

The FEA is performed according to the following algorithm:

1. Create a rectangular area with length and width ratio *m* to *n*.
2. Define two materials: ceramic and air (inside voids), with appropriate thermal conductivities [2.5 W/m/K (Ref 7) and 0.026 W/m/K (Ref 22), respectively, for the YSZ case].
3. Mesh the area with $m \times n$ elements, where $m \times n$ are the original height and width of the image.
4. Assign material properties to each element, according to the image-based material matrix.
5. Apply boundary conditions for through-thickness thermal conductivity (these are isothermal upper and lower boundaries and adiabatic left and right boundaries); for the in-plane direction the boundary conditions are rotated 90°. The difference between the two isotherms will influence the heat flux but not the thermal conductivity result. Hence, the isotherms can be set to be any two distinct values around an interested temperature, for example, 25 and 15 °C for modeling at ambient temperature.
6. Calculate the vertical heat flux of each element for through-thickness thermal conductivity modeling or horizontal heat flux for the in-plane direction. The heat flux of each element is proportional to the isotherm difference.
7. Calculate the effective through-thickness thermal conductivity calculated by averaging the heat flux of each element.

Figure 2(a) is an original grayscale image (1024 × 768 total pixels) of a YSZ cross section. To simulate through-thickness thermal conductivity, the boundary conditions are taken as isothermal for the upper and lower boundaries, and as insulated (adiabatic) for the left- and right-side boundaries. For steady-state conditions, the heat flow through any horizontal plane [actually, a horizontal line in the two-dimensional (2D) image] will be the same and equal to the total heat flow due to energy conservation. As a consequence, the heat flux through the pores and cracks is low due to the low air thermal conductivity (0.026 W/m/K), while the heat flux in the YSZ adjacent to the pores and cracks increases. This can be observed by comparing the topology image in Fig. 2(a) and the vertical heat flux contour plot in Fig. 2(b).

By changing the isotherms for the upper and lower boundaries, the heat flow, heat flux, and spatially resolved thermal conductivity can be determined. In Fig. 2(b), black and white represent the lowest and highest heat fluxes, respectively. From Fig. 2, it is seen that the pores and cracks are important for thermal resistance: the heat flux is reduced where the pores and cracks appear. In addition, in the regions immediately above

and below a pore or crack the heat flux is reduced; however, along the side areas of the same pore or crack the heat flux increases.

3.1 Effect of Threshold Level

In IA, a different thresholding selection for images will cause a different thermal conductivity modeling result. The sensitivity of thermal conductivity on thresholding is investigated by artificially changing the threshold level for binary image conversion. A change of 20 units in the threshold level, which makes a significant difference on a scale of 0 to 255, gives a 5% difference in the FEA thermal conductivity results. This means that the image-based FEA modeling technique is not sensitive to a slight change in the threshold level.

3.2 Dependence on Coating Location

It is also interesting to note that images obtained from different regions of the same coating yield similar porosity and thermal conductivity predictions. This makes it possible to model and predict coating thermal conductivity by averaging results from only a few images taken from distinct locations in the coating. To illustrate this, 10 distinct images were taken from different locations in the same YSZ coating. The calculation of porosity and thermal conductivity results in an average porosity of 7.6% with a standard deviation of 10% and an average thermal conductivity of 1.9 W/m/K with a standard deviation of 5%.

3.3 Dependence on Image Magnification and Image Size

In IA and microstructure modeling (Ref 25-27), the magnification (or equivalently the size of the coating that is imaged) used can have a significant impact on the resulting analysis. Images that are highly magnified result in a loss of global coating information, while images with too low a magnification cannot accurately capture the detailed microstructure at small scales. It is thus important to strike a balance between local and global information, and use the appropriate magnification, while also considering computational requirements (Ref 7).

In this work, the effects of magnification and size are investigated in two ways. First, images are taken at the same site of a coating but at different magnification levels. It is found that higher magnifications result in larger predicted thermal conductivity values. For example, average thermal conductivity results for ×10,000 images were 5% larger than those of ×1000 images of the same coating location. This indicates that images obtained at high magnifications lose global information, for example, large pores, and thus tend to increase the thermal conductivity results. In the second approach, a single image at a given magnification is divided into nine smaller equal-sized images and the finite-element model is applied to each subimage independently. Using this approach, a standard deviation of 5% of the average values was found across the subimages. Interestingly, the average value of the nine thermal conductivity results is very close to the thermal conductivity modeling result for the large image. This suggests that the largest images possible (i.e., highest number of pixels) within the limits of the imaging system should be used. In this work, the uncertainty of the predicted values is estimated to be the combination of the image and location uncertainties (i.e., 10% for all measurements).

4. Coating Thermal Conductivity Measurements

To compare model predictions to actual coating values, measurements of thermal conductivity were made. Room temperature thermal conductivity measurements were made using a Holometrix microflash Laser Flash apparatus manufactured by Netzsch Instruments Inc. (Estes Park, CO), which operates according to ASTM standard E1461 (Ref 28). To measure thermal conductivity, the Holometrix instrument uses a high-power, short-pulse laser to heat the bottom surface of a thin specimen. The heat transferred through the specimen results in a temperature rise at the top surface that is measured by an infrared (IR) detector (Ref 29). Analysis of the bottom-surface temperature time-varying history allows the determination of thermal diffusivity. Specific heat can be measured with the laser flash method by comparing the temperature rise of the sample to the temperature rise of a reference sample of known specific heat tested under the same test conditions. This temperature rise is recorded during the diffusivity measurement, so the specific heat can be calculated from the same data. The apparent density of the sample was obtained by measuring dimensions and weight. The thermal conductivity is calculated from thermal diffusivity, specific heat, and density.

The Holometrix instrument can measure both through-thickness and in-plane direction thermal conductivity for free-standing coatings. For through-thickness measurement, the shape of the coating specimen is a thin disk with a diameter of 12.7 mm and thickness of 0.3 to 2 mm. During the measurement, the bottom-surface of the sample is uniformly irradiated by the laser pulse and the temperature-time is recorded for the central point on the other side. For an in-plane measurement, a square-shaped sample (25.4 × 25.4 mm) is required, and the laser pulse only irradiates the central region of the bottom surface. The temperature is recorded on the backside of the film using an IR detector, and the measured temperature history can then be used to estimate thermal diffusivity and conductivity.

The standard deviation of this technique using the Holometrix instrument has been characterized by Chi et al. (Ref 30). The standard deviation of thermal conductivity measurement for the same coating is 8%. In this work, the standard deviation for through-thickness thermal conductivity measurement is typically 8%, which is the value used for all measurements in this work.

5. Results and Discussions

Using the techniques discussed above, thermal conductivity of thermal sprayed ZrO_2-8wt.%Y_2O_3, Mo, and Ni-5wt.%Al coatings are obtained from both simulation and experiment. Each coating system is discussed in detail below.

5.1 Yttria-Stabilized Zirconia Coatings

The YSZ coatings are often exposed to very high temperatures (up to 1200 °C) and/or multiple thermal cycles for long periods (i.e., hundreds to thousands of hours) when used as TBCs for engineering systems (e.g., in turbine engines). The thermal behavior after heat treatment or annealing is thus important and must be considered for its effect on long-term coating

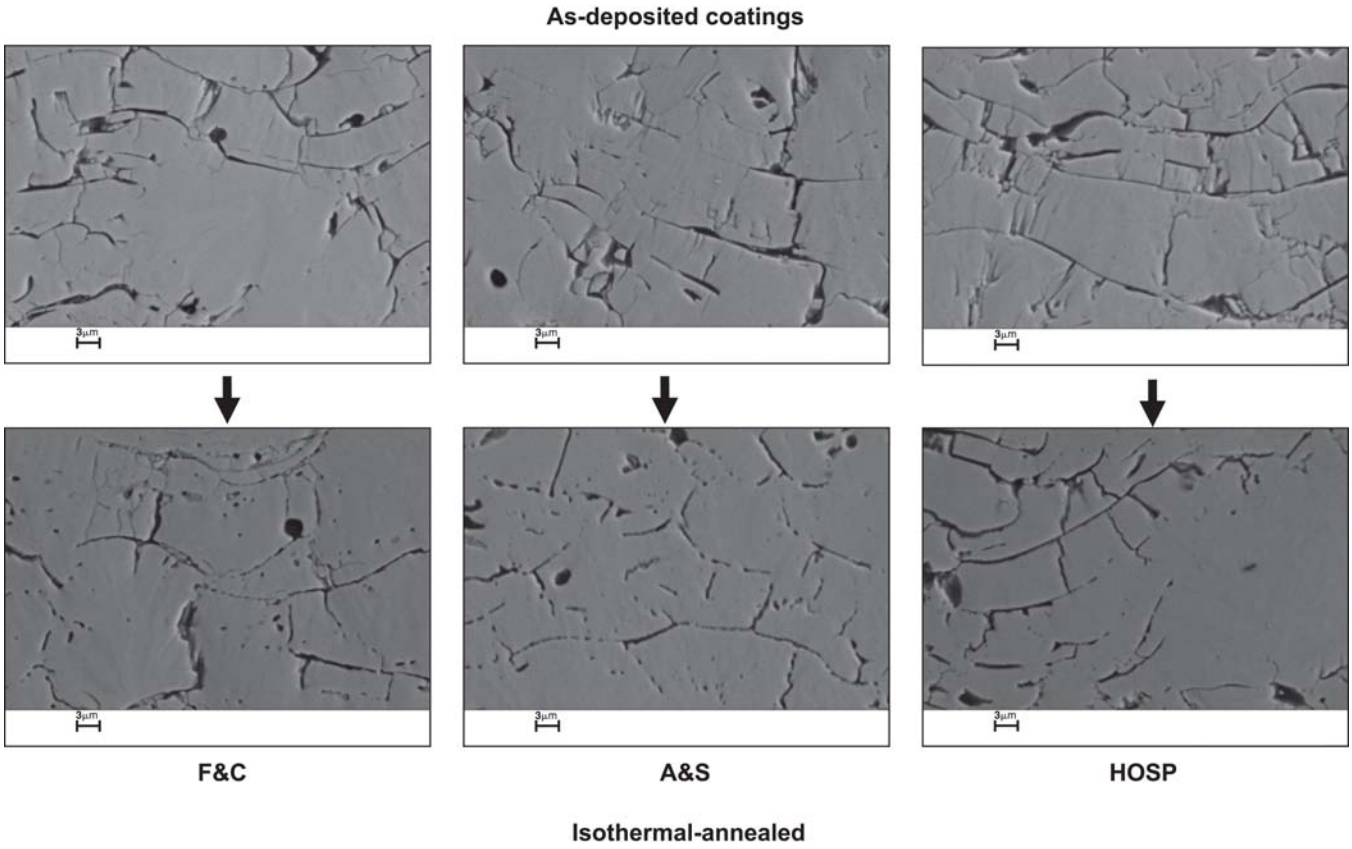

Fig. 3 SEM image of YSZ coatings before and after annealing

Table 1 Thermal conductivity of YSZ coatings (bulk value = 2.5 W/m/K)

	Through-thickness thermal conductivity, W/m/K			In-plane thermal conductivity, W/m/K		
Coatings	**Experiment**	**FEA**	**Difference**	**Experiment**	**FEA**	**Difference**
HOSP as-sprayed	1.10 ± 0.09	1.32 ± 0.13	20%	0.84 ± 0.07	1.60 ± 0.16	90%
HOSP annealed	1.30 ± 0.10	1.42 ± 0.14	9%	1.10 ± 0.09	1.63 ± 0.16	48%
F&C as-sprayed	1.23 ± 0.10	1.56 ± 0.16	27%	1.49 ± 0.12	1.78 ± 0.18	19%
F&C annealed	1.85 ± 0.15	1.78 ± 0.18	−4%	1.65 ± 0.13	1.90 ± 0.19	15%
A&S as-sprayed	1.12 ± 0.09	1.75 ± 0.18	56%	NA	1.46 ± 0.15	NA
A&S annealed	1.43 ± 0.11	1.77 ± 0.18	24%	NA	1.90 ± 0.20	NA

Note: NA, not applicable; HOSP, hollow sphere; F&S, fused and crushed; A&S, agglomerated and sintered

properties. Thermal conductivity modeling and measurement are performed for three types of YSZ coatings both before and after annealing made from fused and crushed, agglomerated and sintered, and plasma-densified hollow sphere powders. The annealing heat treatment was the same for all coatings (225 h at 1200 °C), after which the coating is slowly cooled to room temperature to avoid additional fracture. Figure 3 shows the microstructure images of the three types of YSZ coatings before and after annealing (note that the before and after images represent different locations on the coating). For the as-deposited coatings, the pore and crack network seen in the cross-sectional images is clear and continuous, while the pores and cracks in the annealed coating images are discontinuous and appear to be closing. This geometry change can alter the thermal conductivity of the coatings. The model and measurement data for YSZ coating thermal conductivity before and after annealing are shown in Table 1 and Fig. 4.

It can be seen that after long-term annealing the thermal conductivity data increased for both finite-element and measurement results. As mentioned before, this is due to the microstructure changes and boundary vanishing. Previous work has indicated that the porosity will also decrease after long-term annealing (Ref 7, 10).

As can be seen in the preceding results, a deviation can be found between the modeling and the experimental data. This may be due to a variety of factors including: (a) inadequate resolution in the SEM images, which is unable to accurately capture all of the fine cracks and interfaces, especially in the nanoscale, which are thermal barrier to the heat flow and will lower the computed thermal conductivity; (b) 2D effect, because, strictly speaking, thermal conductivity is a three-dimensional (3D) property and relies on 3D microstructure network and the 2D microstructure image, which is an approximation of the actual 3D structure of a thermal sprayed coating, may lead to signifi-

cant errors; (c) other thermal mechanisms, such as radiation and phonon and photon scattering, which are not included in the simple model; and (d) for the bulk thermal conductivity determination, the bulk value in this work is chosen as 2.5 W/m/K, which is the same as that in the study by Wang et al. (Ref 7). However, the result in the study by Raghavan and Wang (Ref 16) shows that the value was nearly 2.25 W/m/K. A more accurate bulk value, which can be obtained by long-term annealing, will help to decrease the deviation between the simulation and experiment.

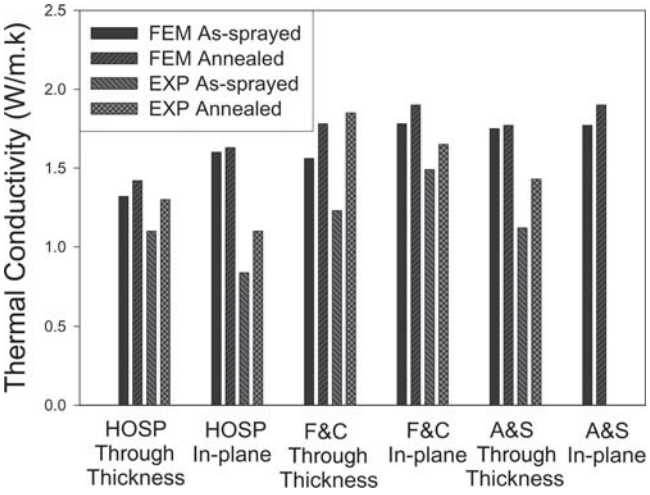

Fig. 4 Modeling and experiment results for YSZ coating thermal conductivity before and after annealing for both the through-thickness and in-plane directions

5.2 Molybdenum Coating

Figure 5 shows the original grayscale and the black-and-white images in which the white area is molybdenum and the black area is air (i.e., only a small amount of oxidation). The thermal conductivity of pure molybdenum is very high (142 W/m/K), compared with the thermal conductivity of air. The

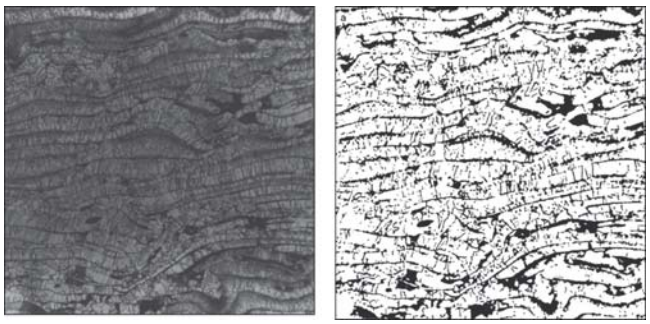

Fig. 5 Grayscale and binary images for Mo coating

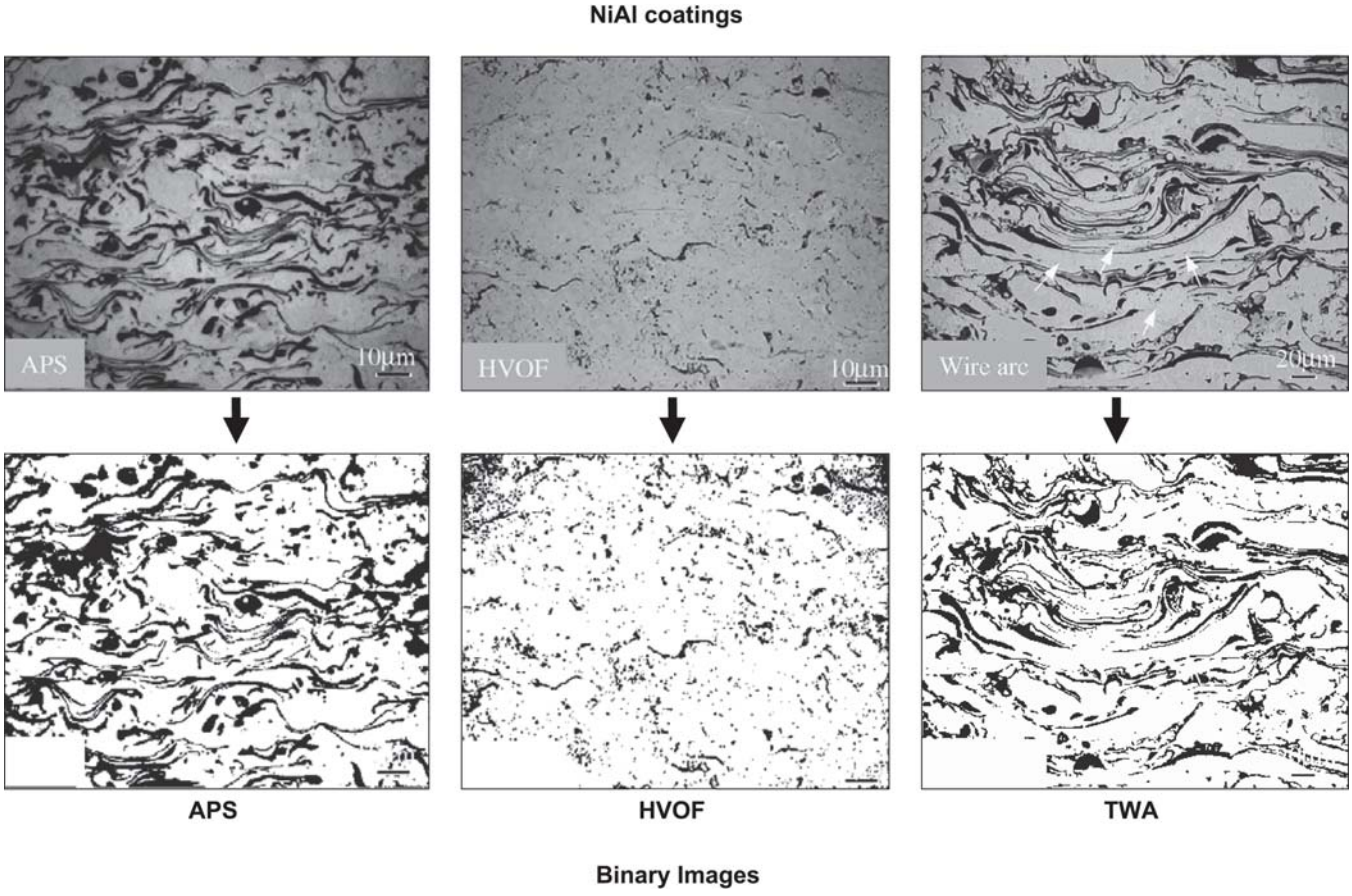

Fig. 6 Grayscale and black-and-white images for Ni-5wt.%Al coatings

Table 2 Thermal conductivity of Mo coating (bulk value = 142 W/m/K)

Through-thickness thermal conductivity, W/m/K			In-plane thermal conductivity, W/m/K		
Experiment	FEA(a)	Difference	Experiment(a)	FEA(a)	Difference
15.0 ± 0.8	10.0 ± 2.0	−33%	40.3 ± 3.2	31.0 ± 6.2	−23%

(a) Values given as mean ± standard deviation

Table 3 Thermal conductivity of Ni-5wt.%Al coatings (bulk value = 80 W/m/K)

	Through-thickness thermal conductivity, W/m/K			In-plane thermal conductivity, W/m/K		
Coatings	Experiment(a)	FEA(a)	Difference	Experiment	FEA(a)	Difference
TWA	17.0 ± 0.9	10.1 ± 2.0	−40.5%	NA	29.5 ± 5.9	NA
HVOF	22.2 ± 1.1	51.4 ± 10.3	132%	NA	54.7 ± 11.0	NA
APS	10.7 ± 0.5	7.5 ± 1.5	−30%	NA	15.3 ± 3.1	NA

Note: NA, not applicable. (a) Values given as mean ± standard deviation

results of the model and experimental values of thermal conductivity are listed in Table 2. It can be seen that the modeling results capture the same trend in the experiments for the thermal conductivities in two perpendicular directions (through-thickness and in-plane).

5.3 NiAl Coatings

Figure 6 shows the original grayscale and the processed black-and-white images for Ni-5wt.%Al coating for three respective processing techniques: air plasma spraying (APS); high-velocity oxyfuel (HVOF) spraying; and twin wire-arc (TWA) spraying. Compared with molybdenum, Ni-5wt.%Al is more readily oxidized, hence the oxide likely represents a non-negligible fraction of the coating cross section. The distribution of each element in the coating is quite complicated (Ref 19). Similar to the case with Mo, the black area in the binary image is assigned to the air property, although this region may also contain oxide as well. The results of thermal conductivity are listed in Table 3. Better agreement is expected by using a more detailed model that includes the oxide, air space, and material independently. As can be seen in Table 3, the difference between experiment and FEA results for the HVOF case is positive, while those of TWA and APS cases are negative. This is likely due to the different nature of the processing techniques for each coating and requires further investigation.

6. Conclusions

This work presents an IA and finite element-based approach, which is not sensitive to slight changes in the threshold level, to predict the thermal conductivity of thermal spray coatings from SEM images of the coating microstructure. Comparisons are made between modeling and experimental values, which were obtained using the laser flash method. For YSZ coatings, the FEA model captures the trends for through-thickness and in-plane thermal conductivities both before and after annealing. The modeling results for YSZ coating thermal conductivity are generally higher than those for the experimental data. For Mo coatings, the results of FEA are lower than those of experiments. For Ni-5wt.%Al coatings, different trends are found in the HVOF case and the TWA or APS case. This work shows that the image-based technique is an effective tool for assessing the thermal conductivity of thermal spray coatings. However, the discrepancy in the comparison of predictions and experiments shows that this technique requires further investigation.

Acknowledgment

The authors gratefully acknowledge support for this work from the National Science Foundation under the Material Research Science and Engineering Center (MRSEC) program, award DMR-0080021.

References

1. W.J. Brindley, Properties of Plasma-Sprayed Bond Coats, *J. Thermal Spray Technol.,* 1997, **6,** p 85-90
2. H. Herman, S. Sampath, and R. McCune, Thermal Spray: Current Status and Future Trends, *MRS Bull.,* 2000, **25,** p 17-25
3. R. McPherson, A Model for the Thermal-Conductivity of Plasma-Sprayed Ceramic Coatings, *Thin Solid Films,* 1984, **112,** p 89-95
4. S. Sampath, X.Y. Jiang, J. Matejicek, A.C. Leger, and A. Vardelle, Substrate Temperature Effects on Splat Formation, Microstructure Development and Properties of Plasma Sprayed Coatings: Part I. Case Study for Partially Stabilized Zirconia. *Mater. Sci. Eng. A,* 1999, **272,** p 181-188
5. F. Cernuschi, S. Ahmaniemi, P. Vuoristo, and T. Mantyla, Modelling of Thermal Conductivity of Porous Materials: Application to Thick Thermal Barrier Coatings, *J. Eur. Ceram. Soc.,* 2004, **24,** p 2657-2667
6. I. Sevostianov and M. Kachanov, Modeling of the Anisotropic Elastic Properties of Plasma-Sprayed Coatings in Relation to Their Microstructure, *Acta Mater.,* 2000, **48,** p 1361-1370
7. Z. Wang, A. Kulkarni, S. Deshpande, T. Nakamura, and H. Herman, Effects of Pores and Interfaces on Effective Properties of Plasma Sprayed Zirconia Coatings, *Acta Mater.,* 2003, **51,** p 5319-5334
8. S. Deshpande, A. Kulkarni, S. Sampath, and H. Herman, Application of Image Analysis for Characterization of Porosity in Thermal Spray Coatings and Correlation With Small Angle Neutron Scattering, *Surf. Coat. Technol.,* 2004, **187,** p 6-16
9. A. Kulkarni, Z. Wang, T. Nakamura, S. Sampath, A. Goland, H. Herman, J. Allen, J. Ilavsky, G. Long, J. Frahm, et al., Comprehensive Microstructural Characterization and Predictive Property Modeling of Plasma-Sprayed Zirconia Coatings, *Acta Mater.,* 2003, **51,** p 2457-2475
10. O. Lavigne, Y. Renollet, M. Poulain, C. Rio, P. Moretto, P. Brännvall, and J. Wigren, Microstructural Characterisation of Plasma Sprayed Thermal Barrier Coatings by Quantitative Image Analysis, *Quantitative Microscopy of High Temperature Materials Conference,* November 22-24, 1999 (Sheffield, UK), Proc. International, 1999
11. M. Poulain, J.M. Dorvaux, O. Lavigne, R. Mévrel, Y. Renollet, and C. Rio, Computation of Thermal Conductivity of Porous Materials Applications to Plasma Sprayed TBCs, *Turbomat 2002 International Symposium on Advanced Thermal Barrier Coatings and Titanium Aluminides for Gas Turbines 2002,* June 17-19, 2002 (Bonn, Germany), Turbomat

12. L. Pawlowski and P. Fauchais, Thermal Transport-Properties of Thermally Sprayed Coatings, *Int. Mater. Rev.,* 1992, **37,** p 271-289
13. B.R. Marple and R.S. Lima, Process Temperature/Velocity-Hardness-Wear Relationships for High-Velocity Oxyfuel Sprayed Nanostructured and Conventional Cermet Coatings, *J. Thermal Spray Technol.,* 2005, **14,** p 67-76
14. R.E. Taylor, Thermal Conductivity Determinations of Thermal Barrier Coatings, *Mater. Sci. Eng. A,* 1998, **245,** p 160-167
15. P.G. Klemens and M. Gell, Thermal Conductivity of Thermal Barrier Coatings, *Mater. Sci. Eng. A,* 1998, **245,** p 143-149
16. S. Raghavan, H. Wang, R.B. Dinwiddie, W. Porter, and M.J. Mayo, The Effect of Grain Size, Porosity and Yttria Content on the Thermal Conductivity of Nanocrystalline Zirconia, *Scripta Mater.,* 1998, **39,** p 1119-1125
17. J.R. Nicholls, K.J. Lawson, A. Johnstone, and D.S. Rickerby, Methods to Reduce the Thermal Conductivity of EB-PVD TBCs, *Surf. Coat. Technol.,* 2002, **151,** p 383-391
18. S.F. Wayne, S. Sampath, and V. Anand, Wear Mechanisms in Thermally-Sprayed Mo-Based Coatings, *Tribol. Trans.,* 1994, **37,** p 636-640
19. S. Sampath, X.Y. Jiang, J. Matejicek, L. Prchlik, A. Kulkarni, and A. Vaidya, Role of Thermal Spray Processing Method on the Microstructure, Residual Stress and Properties of Coatings: An Integrated Study for Ni-5 wt.%Al Bond Coats, *Mater. Sci. Eng. A,* 2004, **364,** p 216-231
20. M. Friis, "A Methodology to Control the Microstructure of Plasma Sprayed Coatings," Ph.D. dissertation, Lund University, Lund, Sweden
21. J. Maxwell-Garnett, Colours in Metal Glasses and in Metallic lms, *Philos. Trans. R. Soc. Lond.on, Ser. B.,* 1904, **203,** p 385-420
22. D.R. Lide, *CRC Handbook of Chemistry and Physics 1913-1995,* 75th ed., CRC Press, Boca Raton, FL
23. National Institutes of Health, NIH Image version 1.62, http://rsb.info.nih.gov/nih-image/, National Institutes of Health, Bethesda, MD
24. G. Antou, G. Montavon, F. Hlawka, R. Bolot, A. Cornet, C. Coddet, and F. Machi, Thermal and Mechanical Properties of Partially Stabilized Zirconia Coatings Manufactured by Hybrid Plasma Spray Process, *High Temp. Mater. Proc.,* 2005, **9,** p 109-125
25. P. Louis and A.M. Gokhale, Application of Image-Analysis for Characterization of Spatial Arrangements of Features in Microstructure, *Metall. Mater. Trans. A,* 1995, **26,** p 1449-1456
26. H. Singh and A.M. Gokhale, Visualization of Three-Dimensional Microstructures, *Mater. Charact.,* 2005, **54,** p 21-29
27. M. Friis, C. Persson, and J. Wigren, Influence of Particle In-Flight Characteristics on the Microstructure of Atmospheric Plasma Sprayed Yttria Stabilized ZrO2, *Surf. Coat. Technol.,* 2001, **141,** p 115-127
28. "Standard Test Method for Thermal Diffusivity of Solids by the Flash Method," 1461-01 AE, *Annual Book of ASTM Standards,* ASTM
29. "Standard Test Method for Thermal Diffusivity of Solids by the Flash Method," E 1461-01, *Annual Book of ASTM Standards,* ASTM, vol 14-02
30. W. Chi, S. Sampath, and H. Wang, Ambient and High Temperature Thermal Conductivity of Thermal Sprayed Coatings, *Building on 100 Years of Success: Proceedings of the 2006 International Thermal Spray Conference,* B.R. Marple, M.M. Hyland, U.-Ch. Lau, R.S. Lima, and J. Voyer, Ed., May 15-18, 2006 (Seattle, WA), ASM International, 2006